







Element-selective local structural analysis around B -site cations in multiferroic $\text{Pb}(\text{Fe}_{1/2}\text{Nb}_{1/2})\text{O}_3$ using x-ray fluorescence holography

K. Kimura ^{1,*} D. Urushihara,^{2,†} R. Kondo,¹ Y. Yamamoto,¹ A. K. R. Ang ¹ T. Asaka ^{2,3} N. Happo ⁴ T. Hagihara,¹ T. Matsushita ⁵ H. Tajiri,⁶ H. Miyazaki,¹ K. Ohara,⁶ M. Iwata ¹ and K. Hayashi^{1,3}

¹Department of Physical Science and Engineering, Nagoya Institute of Technology, Nagoya 466-8555, Japan

²Division of Advanced Ceramics, Nagoya Institute of Technology, Nagoya 466-8555, Japan

³Frontier Research Institute for Materials Science, Nagoya Institute of Technology, Nagoya 466-8555, Japan

⁴Department of Computer and Network Engineering, Hiroshima City University, Hiroshima 731-3194, Japan

⁵Graduate School of Science and Technology, Nara Institute of Science and Technology, Ikoma, Nara 630-0192, Japan

⁶Japan Synchrotron Radiation Research Institute(JASRI), SPring-8, 1-1-1 Kouto, Sayo, Hyogo 679-5198, Japan



(Received 30 May 2021; revised 12 August 2021; accepted 14 September 2021; published 4 October 2021)

X-ray fluorescence holography (XFH) measurements were carried out for multiferroic $\text{Pb}(\text{Fe}_{1/2}\text{Nb}_{1/2})\text{O}_3$ (PFN) single crystal to investigate variations in the local structures around Nb ions with decreasing temperature from 300 to 100 K, in combination with single-crystal x-ray diffraction (XRD) experiments. We find that the Nb–Pb correlation is more significantly changed by cooling than the average structure derived from the single-crystal XRD experiments, indicating a mobile feature of Nb ions. Also, we analyze previously obtained XFH results around Fe ions in detail for comparison with those around Nb ions. In contrast to the case of Nb ions, the variation in the Fe–Pb correlation with decreasing temperature is well explained by the average structure from 300 K down to the Néel temperature of about 150 K. On the other hand, a remarkable positional fluctuation between Fe and Pb ions is observed at 100 K, which is evaluated to be 90% larger than that between Nb and Pb ions. This observation strongly indicates the presence of spin-lattice coupling in PFN. The present study clearly elucidates the differences of local environment around the Nb ions from that around the Fe ions located at the same B -site.

DOI: [10.1103/PhysRevB.104.144101](https://doi.org/10.1103/PhysRevB.104.144101)

I. INTRODUCTION

Lead-based complex perovskite materials, expressed as $\text{Pb}(\text{B}_x\text{B}'_{1-x})\text{O}_3$ ($0 < x < 1$), have been receiving much attention because this series of materials exhibits various remarkable properties depending on the combination of the B -site elements, such as the extremely high piezoelectric performance of $\text{Pb}(\text{Zr}, \text{Ti})\text{O}_3$ [1] and the relaxor behavior of $\text{Pb}(\text{Mg}_{1/3}\text{Nb}_{2/3})\text{O}_3$ [2]. These properties are strongly related to the lattice distortions, which is caused by shifts of the constituent elements from their ideal positions. Therefore, structural information about the B -site elements is important to understand the microscopic origin of the properties of each $\text{Pb}(\text{B}_x\text{B}'_{1-x})\text{O}_3$ compound.

Lead iron niobate, $\text{Pb}(\text{Fe}_{1/2}\text{Nb}_{1/2})\text{O}_3$ (PFN) [3], is one of the $\text{Pb}(\text{B}_x\text{B}'_{1-x})\text{O}_3$ -type complex perovskite compounds that has been extensively investigated due to its multiferroic property, that is, the appearance of the ferroelectric and the antiferromagnetic orderings below the Curie and the Néel (T_N) temperatures of about 385 and 150 K, respectively [3–5]. In particular, numerous studies have been performed to investigate the coupling of these two orderings, which is important to understand the mechanism of the so-called magnetoelectric

effect [6]. The presence of such a coupling was demonstrated in the temperature dependence of the dielectric constant, which exhibits an abrupt jump at T_N [7]. The B -site of PFN is randomly occupied by the magnetic and nonmagnetic elements of Fe and Nb, which should play a key role in inducing the multiferroicity and the magnetoelectric effect.

In order to understand the origin of the multiferroic property of PFN, various structural studies have been performed using diffraction techniques [8–14]. These studies have investigated the temperature dependence of the crystal structure. In a powder x-ray diffraction (XRD) study [12], a negative thermal expansion was reported below T_N , while the symmetry of the crystal structure remained monoclinic (Cm space group) across T_N . Furthermore, the neutron diffraction study performed by Matteppanavar *et al.* [14] reported a sudden decrease in the lattice volume by cooling across T_N , although negative thermal expansion was not observed. On the other hand, another neutron diffraction study [13] has not detected any distinctive variation in the lattice constants near T_N . These contradictory results indicate complicated structural features of PFN.

In addition to the diffraction methods, pair distribution function (PDF) analyses have been carried out using neutrons [13,15]. It was observed that the peak corresponding to the Fe/Nb–Pb pair exhibits a significant variation with decreasing temperature from about 300 K down to 62 K [13] or 75 K [15], whereas that corresponding to the Fe/Nb–O pair remains

*kimura.koji@nitech.ac.jp

†urushihara.daisuke@nitech.ac.jp

almost unchanged in these temperature ranges. Therefore, the correlation between the *B*-site ions and the *A*-site Pb ion is expected to include rich information about the structural variation across T_N . However, the PDF analysis as well as the diffraction technique cannot distinguish the Fe and Nb ions at the *B*-site, despite the fact that the local environments around these elements are supposed to be different due to their different valence states.

Atomic resolution holography is an ideal technique to address this issue [16–18]. This technique provides three-dimensional atomic arrangement around a specific element within a spatial range of about 1 nm and thus has been extensively applied to various materials in order to distinguish local environments around different elements on the same site [19–26]. Moreover, atomic resolution holography can sensitively detect positional fluctuations of atoms [27–34], which has provided useful information on ionic displacements in dielectric materials [35–40]. Therefore, in the case of PFN, local structures around Fe and Nb can be separately analyzed by utilizing this technique. Although x-ray absorption fine structure (XAFS) measurement is also a useful technique for analyzing the local structure around each constituent element, the accessible spatial range of XAFS is smaller than that of atomic resolution holography. Thus, atomic resolution holography can be a more suitable probe to investigate the Fe/Nb–Pb correlation than XAFS. In fact, previous XAFS study on the local structure around Fe in PFN mainly focused on the Fe–O pairs but not on the Fe–Pb pair [41].

Previously, we have investigated the temperature dependence of the local structure around Fe in PFN using x-ray fluorescence holography (XFH) [36], one of the atomic resolution holography techniques. It was found that the atomic image intensity of Pb around Fe becomes weaker below $T_N \sim 150$ K, indicating that the magnetic transition at T_N induces the fluctuation of the Fe–Pb correlation.

In this paper, we apply XFH to PFN in order to investigate the variation in the local structure around Nb with decreasing temperature across T_N . We show that the atomic images corresponding to the Nb–Pb pairs exhibit different temperature dependence from those corresponding to the Fe–Pb pairs. We also perform single-crystal XRD measurements to derive an average crystal structure, which is compared with the element-selective local structures. The obtained results are discussed in relation to the spin-lattice coupling.

II. EXPERIMENT AND ANALYSIS

The PFN single crystal was grown using the flux method. The PbO , Fe_2O_3 , and Nb_2O_5 powders were mixed in the stoichiometric ratio, to which PbO self-flux was added. Then, the mixed powder was sealed in a Pt crucible, which was put in the electronic furnace. The temperature of the furnace was kept at 1423 K for 2 h and then cooled down to 1223 K at a rate of 3.0 Kh^{-1} followed by the further cooling to 1073 K at a rate of 5.0 Kh^{-1} . The details of the sample preparation are described elsewhere. The size of the largest single crystal was about 4 mm, which was used for the XFH measurement.

Furthermore, we also ground a part of the other crystals to perform the powder XRD measurements at BL02B2 of

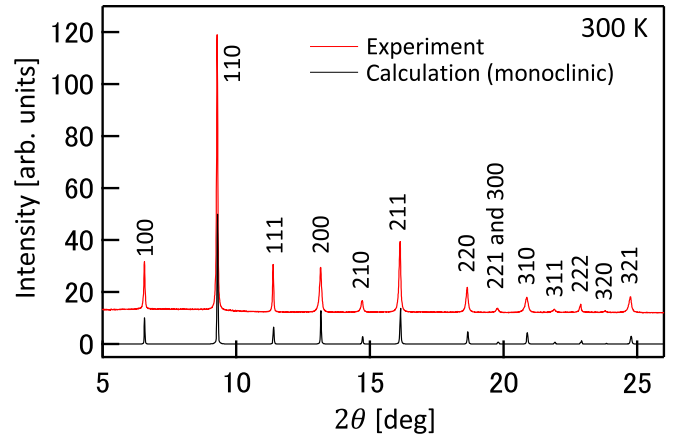


FIG. 1. XRD pattern of the PFN powder. The wavelength of the x-ray is 0.46 \AA . The calculated XRD pattern of monoclinic PFN is also shown.

SPring-8. The measurements were performed at the x-ray wavelength of 0.46 \AA and at room temperature. Figure 1 shows the obtained experimental XRD pattern together with the calculated result. We can confirm that all the peaks are well assigned to those originating from the monoclinic PFN, which assures that the grown crystals are single phase PFN. Here we calculated the XRD pattern using the coordinate of the monoclinic PFN at 300 K derived from the single-crystal XRD measurements, which will be described later.

XFH experiments were carried out at BL13XU of SPring-8 [42,43]. The Nb- $K\alpha$ line (16.6 keV) was analyzed by cylindrical graphite crystals and then detected by an avalanche photodiode detector. The incident x-ray energies were set from 20.0 to 24.0 keV in steps of 1.0 keV, which are above the Nb *K*-edge, 19.0 keV. The ranges of the incident, θ , and azimuthal, ϕ , angles were $0^\circ \leq \theta \leq 75^\circ$ in steps of 1° and $0^\circ \leq \phi \leq 360^\circ$ in steps of 0.25° , respectively. The average fluorescent intensity at each θ and ϕ was at least $\sim 17,000$ counts for each hologram. The details of the experimental setup are described elsewhere [17,18]. The measurements were performed at the temperatures from 100 to 300 K in steps of 50 K. The sample was cooled by a liquid-nitrogen open-flow cooler.

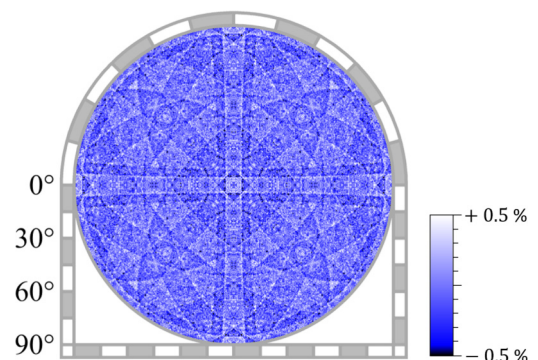


FIG. 2. Nb- $K\alpha$ hologram measured at the incident energy of 20.0 keV and the temperature of 300 K.

TABLE I. Experimental conditions for single-crystal XRD measurements.

Temperature [K]	100	150	200	250	300
2θ range	<61.0	<61.0	<60.2	<60.2	<60.2
Observed reflection	1748	1776	1830	1958	1944
Unique reflection	409	408	406	406	405
R_{int}	0.0211	0.0226	0.0227	0.0225	0.0230
Collection range	$-8 \leq h \leq 8$ $-8 \leq k \leq 8$ $-5 \leq l \leq 5$	$-8 \leq h \leq 8$ $-8 \leq k \leq 8$ $-5 \leq l \leq 5$	$-8 \leq h \leq 8$ $-8 \leq k \leq 8$ $-5 \leq l \leq 5$	$-8 \leq h \leq 8$ $-8 \leq k \leq 8$ $-5 \leq l \leq 5$	$-8 \leq h \leq 8$ $-8 \leq k \leq 8$ $-5 \leq l \leq 5$
$R [F^2 > 3\sigma(F^2)]$	0.0194	0.0212	0.0242	0.0251	0.0248
$wR (F^2)$	0.0517	0.0567	0.0656	0.0790	0.0686

Figure 2 shows the Nb- $K\alpha$ hologram measured at an incident x-ray energy of 20.0 keV at 300 K. Here, symmetry operation was applied using the cubic symmetry to cover all solid angles and to enhance the statistics. Clear standing wave lines are observed, which confirms that the measurements were successfully performed. From the obtained holograms, atomic images are reconstructed using Barton's algorithm [44]. The data processing was done using software "3D-Air-Image" [45]. This software was also used for calculations of hologram patterns based on structural models described in Section IV.

We also performed single-crystal XRD measurements to investigate the average structure from 100 to 300 K in steps of 50 K. The measurements were performed using D8 VENTURE (Bruker) with Mo- $K\alpha$ laboratory x-ray source (50 kV, 1 mA). Table I summarizes the experimental conditions. The lattice constants were calculated based on the SAINT program [46], where we used the Cm (No. 8) space group. Multiscan absorption correction provided by the SADABS program [46] was applied to the experimental data. The initial structural models were derived using the Superflip program based on the charge-flipping algorithm [47]. The JANA2006 program package [48] was used for the crystal structure analyses.

III. RESULTS

A. XFH

Figure 3 shows the reconstructed atomic images of the Pb plane around Nb ions at each temperature. The $\langle 100 \rangle_{\text{cubic}}$ and $\langle 010 \rangle_{\text{cubic}}$ directions are taken as the horizontal and the vertical axes, respectively. Here, mirror indices with the subscript of "cubic" indicate those in the case of the cubic symmetry. The corresponding Pb plane is schematically shown in the lower part of this figure. We can confirm clear atomic images within the circles, which indicate the ideal positions of the Pb ions. In appearance, these atomic images are not significantly dependent on the temperature.

In order to examine the variation in the atomic images with decreasing temperature in more detail, we reconstructed the three-dimensional atomic images of the first nearest neighbor (NN) Pb ion at each temperature, as indicated in Fig. 4. Here, the 85% volume contours are shown. Whereas the shapes of the atomic images are similar from 150 to 300 K, the image at 100 K is stretched in the $\langle 111 \rangle_{\text{cubic}}$ direction. Since T_N is about 150 K, it is reasonable to consider that this structural variation is induced by the transition from the paramagnetic to antiferromagnetic phase.

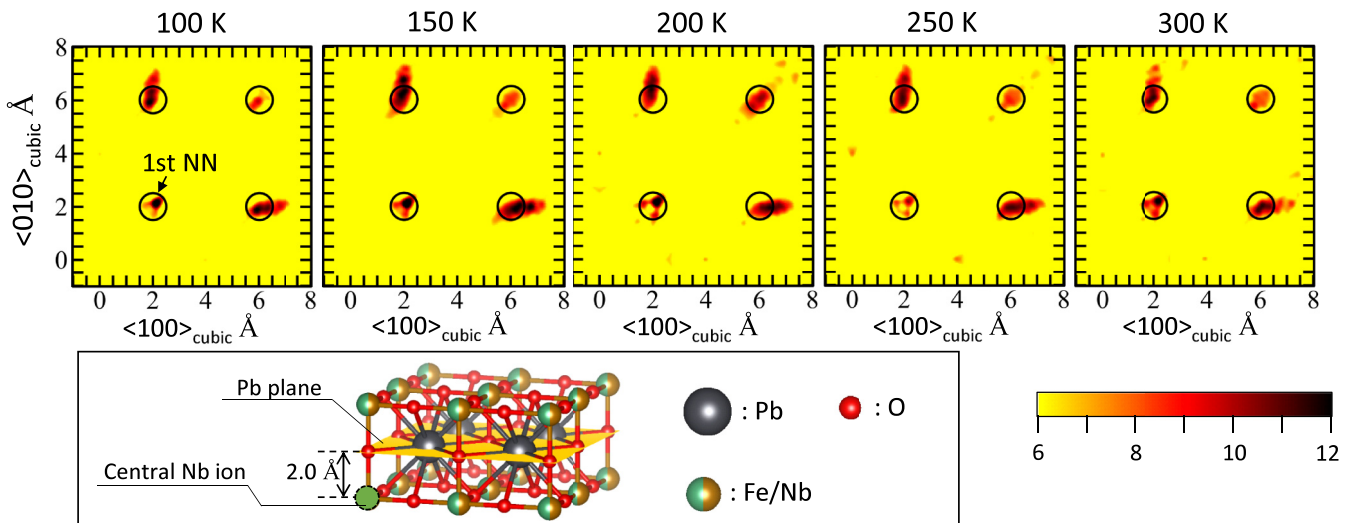


FIG. 3. Reconstructed atomic images of Pb plane around Nb from 100 to 300 K in steps of 50 K. Circles indicate the ideal positions of Pb ions. The corresponding Pb plane is schematically illustrated in the lower part, which was drawn by using VESTA software [49].

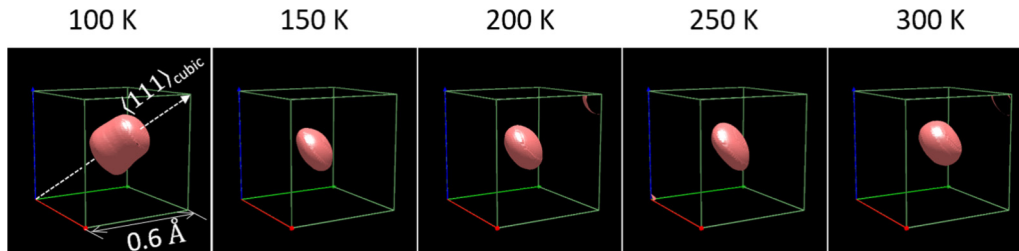


FIG. 4. Three-dimensional atomic images of the first NN Pb ion around Nb from 100 to 300 K in steps of 50 K. The 85% volume contours are displayed.

B. Single-crystal XRD

Table II shows the lattice constants of PFN determined from the single-crystal XRD measurements. The a , b , and c values are in good agreement with the previously reported values [8, 12–14]. The value of β systematically increases with decreasing temperature, which shows that the lattice distortion becomes larger by cooling. In Fig. 5(a), the $a/\sqrt{2}$, $b/\sqrt{2}$, and c values are plotted as a function of temperature. It is observed that the difference between $a/\sqrt{2}$ and $b/\sqrt{2}$ tends to become larger with decreasing temperature, reflecting the enhanced lattice distortion in the lower temperature range. This behavior is consistent with the temperature dependence of β in Fig. 5(b), which deviates from 90° more largely by cooling. On the other hand, the unit cell volume shown in Fig. 5(b) is not systematically dependent on temperature.

Therefore, no significant change in lattice constants is confirmed near the Néel temperature of about 150 K, overall. This observation is different from that in the previous diffraction studies by Singh *et al.* [12] and Matteppanavar *et al.* [14], who reported a negative thermal expansion below T_N and an abrupt drop of the unit cell volume near T_N , but in accordance with the neutron diffraction study performed by Sim *et al.* [13] Thus, the average structure of the presently synthesized sample is not sensitive to the magnetic transition at T_N , in contrast to the local structure around Nb (Fig. 4).

Table III shows the atomic coordinates derived from the single-crystal XRD. Here, the B -site position is taken as the origin. The x and y values of the Pb ion are shifted with decreasing temperature relative to the B -site position, and consequently the deviation from the cubic structure becomes larger. The direction of this shift corresponds to the $\langle 111 \rangle_{\text{cubic}}$ direction.

IV. DISCUSSION

A. Comparison with the average structure

Figure 6 compares the experimental and calculated profiles of the first NN Pb ions around the B -site in the $\langle 111 \rangle_{\text{cubic}}$ direction (Fig. 4) at each temperature. The peak position of the profile at 300 K is taken as the origin of the horizontal r axis. In the result obtained by the XFH measurements [Fig. 6(a)], the peak position systematically shifts to the lower r region to $r = -0.09 \text{ \AA}$ as the temperature decreases to 150 K. In addition, another broad peak appears at around $r = 0.17 \text{ \AA}$ at 150 K, as indicated by the dashed curves, which are Gaussian functions fitted to the experimental profile. By cooling down to 100 K, the position of this peak moves to $r = 0.14 \text{ \AA}$

while that of the other peak remains $r = -0.09 \text{ \AA}$, and consequently the appearance of the profile becomes flat in the region $-0.1 \text{ \AA} \leq r \leq 0.15 \text{ \AA}$. This feature corresponds to the stretched three-dimensional atomic image at 100 K shown in Fig. 4.

Note that the magnitude of the error bar shown in Fig. 6(a) at 300 K is much smaller than the observed temperature dependence of the profiles. The error was evaluated from the signal-to-noise ratio (SNR) given by [50],

$$\text{SNR} \sim \sqrt{2I_{\text{tot}}} \frac{b}{R} X(R),$$

where I_{tot} is the total count of the fluorescent x-rays, b is the scattering amplitude, and R is the distance of the atomic image from the central atom. $X(R)$ represents the effects concerning the real experimental environment, such as wavelength resolution and the mosaicity of the sample. Here we approximated $X(R)$ to 1 for simplicity. From the average fluorescent intensity ($\sim 17,000$) and the measurement conditions for θ and ϕ ($0^\circ \leq \theta \leq 75^\circ$ in steps of 1° and $0^\circ \leq \phi \leq 360^\circ$ in steps of 0.25°), the total count can be calculated as $I_{\text{tot}} \sim 17,000 \times 76/1 \times 360/0.25 \sim 1.86 \times 10^9$; b is the product of the number of electrons in the Pb^{2+} ion (80) and the classical electron radius ($2.8 \times 10^{-5} \text{ \AA}$). R is the distance between the Nb^{5+} ion and the Pb^{2+} ion, that is, $\sim 3.5 \text{ \AA}$. From these values, SNR can be evaluated as ~ 39 , i.e., the error of the atomic image intensity is about $\pm 2.6\%$, which is indicated as an error bar in Fig. 6(a) at 300 K. Therefore, the changes in the profile by cooling is surely caused by local structural changes of PFN.

Figure 6(b) shows the profiles calculated from the average structure. In the calculation, we put Nb at the B -site of the coordinate determined by the single-crystal XRD (Table III). Then, on the basis of this coordinate, we generated a cluster with a radius of 5 \AA having Nb as the central atom. Using this cluster, hologram patterns of fluorescent x-rays from Nb were

TABLE II. Lattice constants of PFN determined from the single-crystal XRD measurements. The Cm space group (No. 8) was used for the structural refinement.

T [K]	a [Å]	b [Å]	c [Å]	β [°]
100	5.6804(2)	5.6647(2)	4.0140(2)	90.222(2)
150	5.6798(2)	5.6663(2)	4.0147(2)	90.195(2)
200	5.6783(2)	5.6670(2)	4.0145(2)	90.164(2)
250	5.6771(2)	5.6679(2)	4.0143(2)	90.140(2)
300	5.6759(2)	5.6688(2)	4.0150(2)	90.107(2)

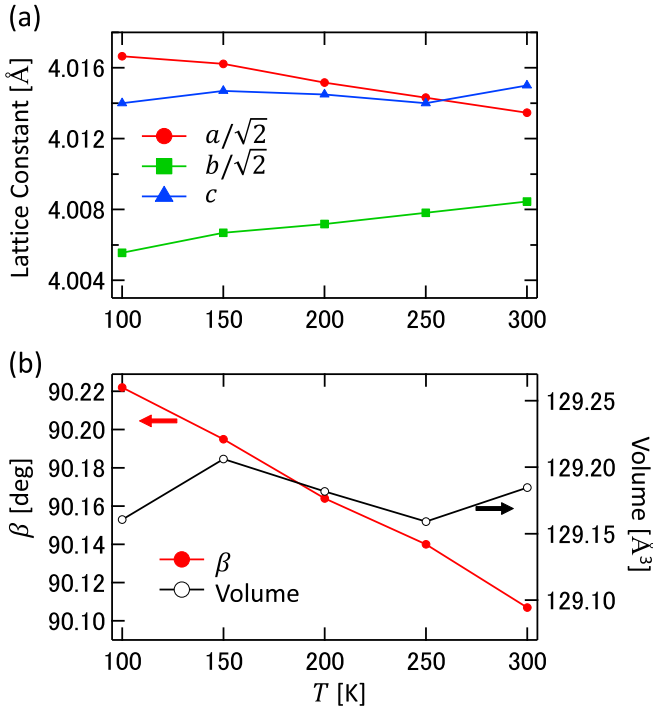


FIG. 5. Temperature dependence of (a) $a/\sqrt{2}$, $b/\sqrt{2}$, c , (b) β and a unit cell volume of PFN determined from single-crystal XRD measurements. The Rietveld structural refinement was done based on the monoclinic structure (Cm space group).

calculated at the incident energies from 20.0 to 24.0 keV in steps of 1.0 keV using the equation described in Refs. [17,18]. From the obtained hologram patterns, the atomic image was reconstructed using Barton’s algorithm [44].

TABLE III. Atomic coordinates x , y , z and the atomic displacement parameter U_{eq} of PFN derived from the single-crystal XRD analysis from 100 to 300 K in steps of 50 K. Fe/Nb sites are fixed.

T [K]	Site	x	y	z	U_{eq} [Å^2]
100	Pb	0.5189(5)	0	0.9799(7)	0.0298(2)
	Fe/Nb	1/2	1/2	1/2	0.0089(3)
	O1	0.4713(12)	1/2	0.020(2)	0.0140(14)
	O2	0.2272(9)	0.2560(8)	0.5315(13)	0.0143(10)
150	Pb	0.5175(6)	0	0.9811(8)	0.0314(2)
	Fe/Nb	1/2	1/2	1/2	0.0093(3)
	O1	0.4717(14)	1/2	0.018(2)	0.016(2)
	O2	0.2275(10)	0.2561(9)	0.5312(14)	0.0150(10)
200	Pb	0.5156(6)	0	0.9827(9)	0.0336(3)
	Fe/Nb	1/2	1/2	1/2	0.0098(3)
	O1	0.474(2)	1/2	0.018(2)	0.017(2)
	O2	0.2290(11)	0.2561(10)	0.528(2)	0.0166(12)
250	Pb	0.5137(7)	0	0.9838(11)	0.0361(3)
	Fe/Nb	1/2	1/2	1/2	0.0104(4)
	O1	0.475(2)	1/2	0.017(2)	0.017(2)
	O2	0.2319(13)	0.2546(12)	0.524(2)	0.0183(14)
300	Pb	0.5120(6)	0	0.9865(9)	0.0386(3)
	Fe/Nb	1/2	1/2	1/2	0.0105(3)
	O1	0.4789(14)	1/2	0.014(2)	0.017(2)
	O2	0.2333(11)	0.2541(10)	0.525(2)	0.0178(11)

It is observed that the peak position of the profile in Fig. 6(b) shifts to the lower r region. This behavior is qualitatively in accordance with the experimental results, but the magnitude of the shift is much smaller. Moreover, the additional peaks in the positive r side observed at 150 and 100 K in the experimental results are not reproduced in Fig. 6(b). These disagreements clearly show the difference of the local structure around Nb from the average structure. Such a difference between local and average structures has been reported in previous PDF studies not only on PFN [13,15] but also on other ferroelectric materials such as $\text{Pb}(\text{Mg}_{1/3}\text{Nb}_{2/3})\text{O}_3$ [51], $\text{Pb}(\text{In}_{1/2}\text{Nb}_{1/2})\text{O}_3$ [52], and $\text{Pb}(\text{Sc}_{1/2}\text{Ta}_{1/2})\text{O}_3$ [53].

In order to improve the agreement, we calculate the profiles based on a Nb shift model as shown in Fig 6(c). In this model, we additionally move the Nb ion in the $\langle 111 \rangle_{\text{cubic}}$ direction below the temperature of 250 K. From Fig. 7, we can confirm the magnitude of the Nb shift in this model. Here, the distances of the six Pb ions from the Nb ions, numbered as (1)–(6), are displayed. The corresponding Pb ions are schematically illustrated on the right, where the direction of the $\langle 111 \rangle_{\text{cubic}}$ shift of the Nb ion is indicated by the arrow. As observed in Fig. 6(c), this model well reproduces the features of the experimentally obtained profiles at 250, 200, and 150 K, that is, the magnitude of the peak shift with decreasing temperature and the additional peak in the positive r region at 150 K. This additional peak is not observed in the case of average structure, since the peaks corresponding to the six Nb–Pb pairs are merged into one in the profile shown in Fig. 6(b). On the other hand, these peaks are split into two in the Nb shift model at 150 and 100 K, because the Pb(2), Pb(4), and Pb(6) ions become more distant from and the other three Pb ions become closer to the Nb ion in this model than in the average structure.

However, the profile in Fig. 6(c) at 100 K is not in good agreement with the experimental result. In particular, the position of the peak in the positive r region is not well reproduced by the Nb shift model, which suggests that another shift is induced for Nb or Pb ions. According to the previous PDF analysis of PFN powder using neutrons [15], the Pb displacement of $(-0.035, -0.023, -0.025)_{\text{mono}}$ (fractional coordinate) was proposed to explain a feature in the PDF at 75 K. (Here, the brackets with the subscript of “mono” indicate the coordinate in the case of monoclinic symmetry.) In the unit of Å , this displacement is $(-0.2, -0.13, -0.1)_{\text{mono}} \text{Å}$. Figure 8 shows the calculated profile using this model, where the magnitude of the displacement was reduced by a factor of 0.63 from the original values, that is, the displacement is expressed as $(-0.13, -0.09, -0.06)_{\text{mono}} \text{Å}$. Here, the average structure at 100 K was used as the original coordinate. It can be observed that the peak positions in both negative and positive r regions agree well with those of the experimental profile at 100 K. This result indicates that the direction of the Pb shift relative to the B -site ions is changed across T_N of about 150 K.

B. Comparison with the local structure around Fe

In our previous study [36], XFH of Fe- $K\alpha$ line was measured at 100, 150, 200, 250, and 300 K. In that study, the energies of the incident x-rays were from 9.0 to 11.5 keV in

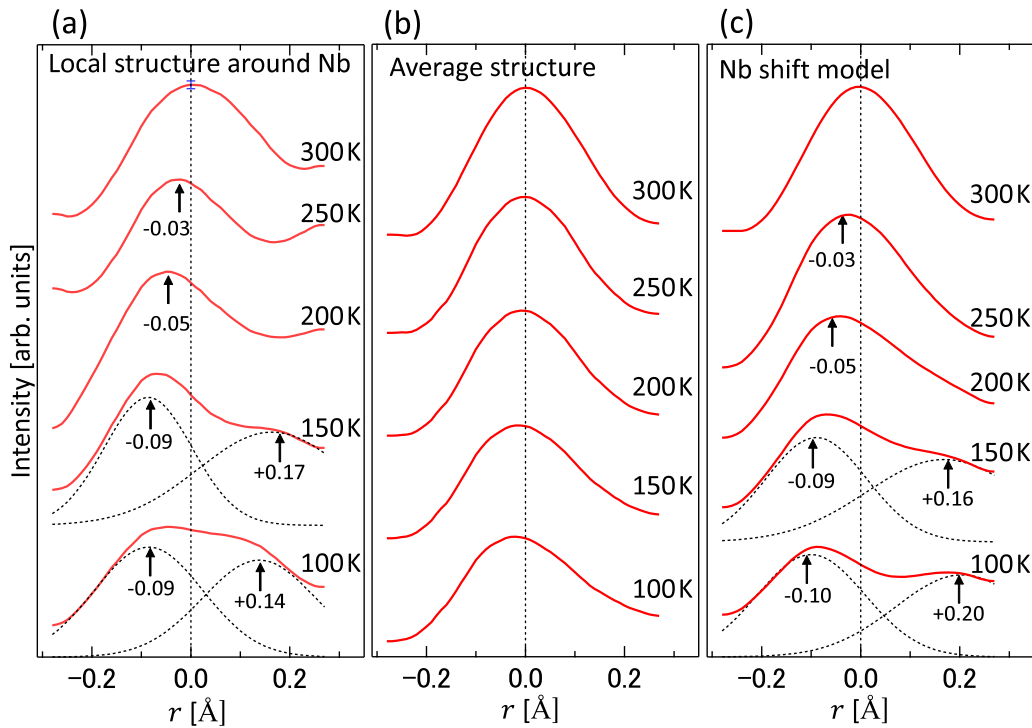


FIG. 6. Profiles of the first NN Pb ion around Nb in the direction of $\langle 111 \rangle_{\text{cubic}}$ at 100, 150, 200, 250, and 300 K. Profiles obtained from (a) XFH results, (b) average structure (single-crystal XRD), and (c) Nb shift model are shown. The peak position of the profile at 300 K is taken as the origin of the horizontal axis. Dashed curves are Gaussians fitted to the profiles. An error bar displayed in (a) at 300 K was evaluated according to Ref. [50].

steps of 0.5 keV, which were lower than the energies used in the present study. Therefore, the spacial resolution of the obtained atomic image around Fe is lower than that around Nb obtained in the present measurements, and thus the shape of the first NN Pb atomic image around Fe was not significantly dependent on the temperature [36]. Instead, an abrupt decrease in the atomic image intensity was observed by cooling

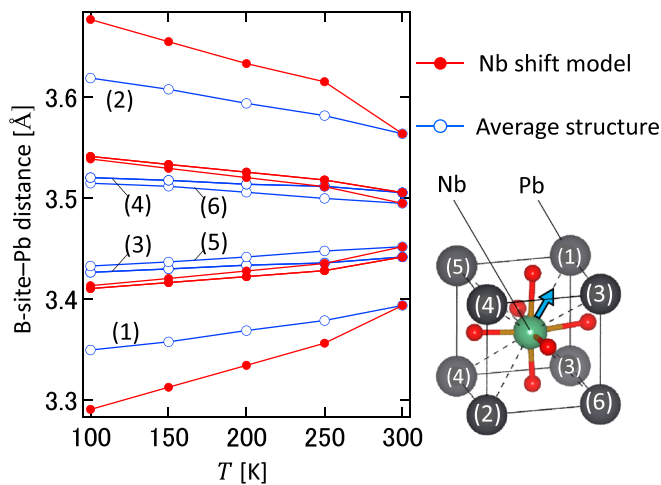


FIG. 7. Temperature dependence of the distance between the Nb and the Pb ions obtained from the average structure and the Nb shift model. Distances of the six Pb ions (1)–(6) from the Nb position are displayed. The corresponding Pb ions are illustrated on the right, which was drawn by using VESTA software [49].

down from 150 to 100 K, whereas no clear variation in the intensity was confirmed in the temperature range from 150 to 300 K. This behavior is shown by the open circles in Fig. 9. Here, the T_N of 156 K is indicated, which was determined by a superconducting quantum interference device magnetometer [36].

In order to ascertain if this behavior can be reproduced by the models described above, we calculated the first NN Pb atomic images at each temperature using the incident x-ray energies from 9.0 to 11.5 keV in steps of 0.5 keV and plotted the intensity of the obtained image as a function of temperature in Fig. 9. The intensities are normalized by the experimental result at 300 K. Since the atomic image intensity

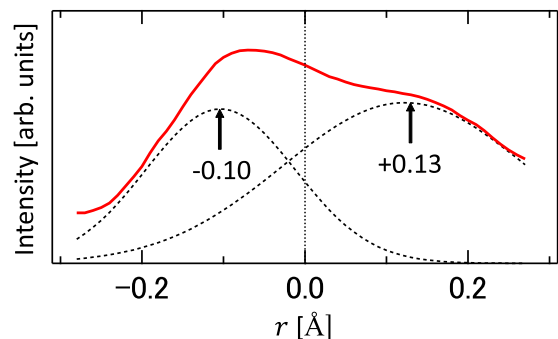


FIG. 8. Calculated profile of the first NN Pb atomic image around Nb. The calculation was done by introducing Pb displacement of $(-0.13, -0.09, -0.06)_{\text{mono}}$ to the average structure at 100 K.

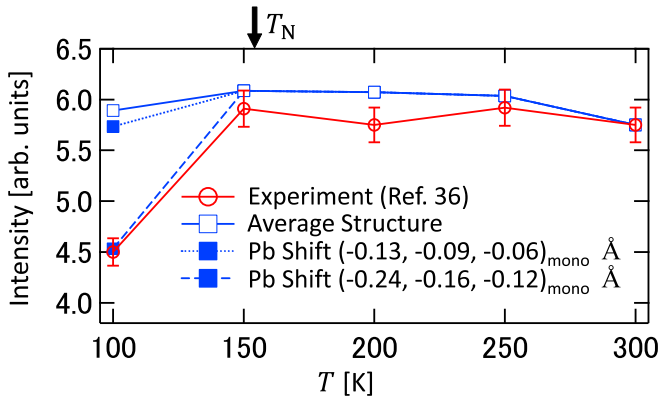


FIG. 9. Temperature dependence of the first NN Pb atomic image intensity around Fe ions. The result of the XFH measurement is shown together with the calculated plots obtained from some structural models. The intensity is normalized by the XFH result at 300 K. The experimental data were taken from Ref. [36].

is sensitive not only to the distortion but also to the positional fluctuations owing to the thermal vibration and structural disorder, we took into account the positional fluctuations by adding a three-dimensional Gaussian distribution to the Pb and Fe atomic positions. Here, the width of the Gaussian was derived from the atomic displacement parameters U_{eq} in Table III.

As indicated by the open squares in Fig. 9, the atomic image intensities obtained from the average structure are almost independent of temperature. This behavior can be explained by two competing effects on the atomic image intensity, i.e., the enhancement of the lattice distortion and the suppression of the thermal vibration with decreasing temperature, which have the effects of reducing and increasing the atomic image intensity, respectively. These effects are canceled out in the case of average structure, and consequently no significant temperature dependence was observed. This temperature dependence agrees well with the experimental results above 150 K, which suggest that the local structure around the Fe ion is similar to the average structure in this temperature range.

These results show that the position of the Fe ion is more stable than that of the Nb ions with the decrease in temperature down to 150 K. This behavior is reasonably understood by the different valence states of the Nb and Fe ions. Since the Nb^{5+} ion is a d^0 transition metal, i.e., d -orbital of the Nb^{5+} ion is empty, there is a strong tendency that the position of Nb^{5+} is displaced from the center of the oxygen octahedron owing to the second-order Jahn Teller effect [54,55]. On the other hand, the Fe^{3+} ion possesses five valence electrons in its $3d$ orbital, and thus this ion can share electron density with surrounding oxygens, resulting in a relatively rigid local structural environment.

At 100 K, however, the average structure cannot reproduce the abrupt drop of the atomic image intensity (Fig. 9). Therefore, a large positional fluctuation between Fe and Pb ions is expected at 100 K. In Ref. [36], the temperature dependence of the B -site atomic image around the Fe^{2+} ion was also investigated, and it was found that the B -site atomic image intensity was not significantly changed at 100 K. Thus, the

weakening of the atomic image intensity at 100 K in Fig. 9 is mainly attributed to the Pb displacement, while the position of the Fe^{3+} ion is relatively stable.

In the case of local structure around Nb, the profile of the first NN Pb ion at 100 K [Fig. 6(a)] was well reproduced by introducing the Pb shift of $(-0.13, -0.09, -0.06)_{mono}$ Å from the average structure. As indicated by a solid square with a dotted line in Fig. 9, this Pb shift results in a decrease in the atomic image intensity, but the magnitude of the decrease is much less than that of the experimental result, which clearly shows that the Pb shift is much larger around the Fe^{3+} ion than around the Nb^{5+} ion. To explain this experimental observation, it is necessary to increase the amount of the Pb shift to $(-0.24, -0.16, -0.12)_{mono}$ Å, as indicated by a solid square with a dashed line. This shift is 90% larger than that predicted around the Nb ion and 20% larger than the previously reported value obtained by the neutron PDF analysis at 75 K [15].

This large difference in the local environments between the Fe^{3+} and Nb^{5+} ions suggests that the chemical arrangement of these ions is not homogeneous. This is because if the Fe^{3+} and Nb^{5+} ions were homogeneously distributed in the B -site of PFN, the effect of the Pb displacement on the atomic image around the Nb^{5+} ions should be similar to that around the Fe^{3+} ions. Therefore, we infer that the chemical inhomogeneity of the B -site ions is present in PFN. This is consistent with a previous study on the Néel temperature of PFN doped with Ba [56], where it was indicated that the Fe ions form antiferromagnetic clusters. Also, Laguta *et al.* [57] showed the presence of the Nb-rich and Fe-rich regions using a nuclear magnetic resonance and an electron paramagnetic resonance technique. In this situation, the Pb shift around the Nb^{5+} ion can be different from those around the Fe^{3+} ion, which can explain the experimental observations.

C. Relation to the magnetic transition at T_N

We can reasonably attribute the observed large local structural variation around the Fe ion at 100 K to the transition from the paramagnetic into the antiferromagnetic phase, considering that the Néel temperature is about 150 K. It was reported in neutron diffraction studies [13,14] that the Fe ions in PFN form a G-type antiferromagnetic order below T_N . In these studies, the B -site ions are virtually approximated to magnetic ions with a magnetic moment smaller than that of the Fe^{3+} ion to express the situation that the B -site is randomly occupied by magnetic and nonmagnetic ions of Fe and Nb. In such an approximation, there is no frustration in forming the antiferromagnetic order. On the other hand, the B -sites next to the Fe ions are not only occupied by the Fe ions but also occupied by the nonmagnetic Nb ions in the real atomic arrangement, where the superexchange interactions among Fe ions via oxygen are interrupted by the insertion of the Nb ions.

In Ref. [58] magnetic ground states were calculated for various chemical arrangements of the B -site. This study took into account not only the effect of the $Fe^{3+}-O^{2-}-Fe^{3+}$ superexchange interaction but also the effect of the second and third NN interactions. Although it was shown that the $Fe^{3+}-O^{2-}-Fe^{3+}$ superexchange interaction is dominant over the second and third NN interactions [58], the interactions

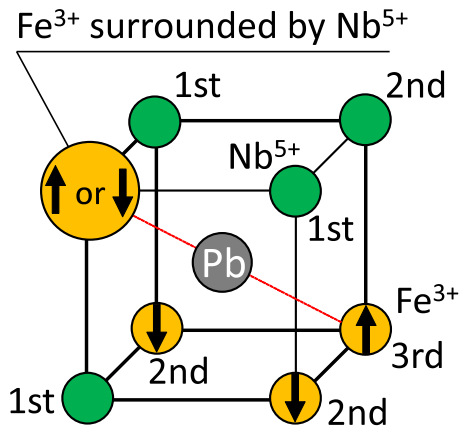


FIG. 10. An example of the B -site atomic arrangement, in which a Fe^{3+} ion is surrounded by Nb^{5+} ions.

among Fe ions become complicated when the first NN B -sites are occupied by Nb ions. Figure 10 illustrates an example of such arrangements. According to Ref. [58], the spin of the isolated Fe^{3+} ion surrounded by the Nb^{5+} ions becomes antiparallel to the spin of the second NN Fe^{3+} ions in the magnetic ground state of this arrangement. On the other hand, the presence of the Fe^{3+} - Pb^{2+} - Fe^{3+} superexchange interaction was indicated in a previous experimental study on the Néel temperature of $(\text{Pb}_{1-x}\text{Ba}_x)(\text{Fe}_{1/2}\text{Nb}_{1/2})\text{O}_3$, that is, the third NN Fe^{3+} ion can interact with the isolated Fe^{3+} ion via lone pair electrons in the Pb^{2+} ion [56]. Under the influence of this interaction, the spin of the isolated Fe^{3+} ion becomes antiparallel to that of the third NN Fe^{3+} ion, which is competing against the magnetic ground states of B -site sublattice predicted in Ref. [58].

Such a frustration can be caused by various chemical arrangements of the B -site besides the arrangement shown in Fig. 10. It is conceivable that the shift of the Pb^{2+} ions is induced below T_N to relax the frustration originating from the complex interactions among Fe^{3+} ions owing to the B -site randomness. As mentioned in the previous subsection, it has been indicated that Fe ions form antiferromagnetic clusters in PFN [56]. Furthermore, according to Ref. [56], the Pb ions can work as a mediator among these clusters through the Fe^{3+} - Pb^{2+} - Fe^{3+} superexchange interaction to form the antiferromagnetic phase at relatively a high temperature of about 150 K in comparison with Pb-free perovskites such as $\text{Ba}(\text{Fe}_{1/2}\text{Nb}_{1/2})\text{O}_3$. Therefore, the Pb shift should occur remarkably around the Fe ions at the surface of the clusters, which is considered to be reflected in the significant weakening of the Pb atomic image intensity around the Fe ion at 100 K (Fig. 9). Here, the size of the clusters is considered to be small, since a formation of a large Fe^{3+} cluster is inconceivable owing to the charge neutrality. Thus, a large part of the Fe ions should be at the surface of the clusters. On the other hand, the Pb shift is expected to be less significant around the Nb ion, since the Fe^{3+} - Pb^{2+} - Fe^{3+} pairs are not always present near the Nb ions, which is consistent with the estimation described above that the Pb shift around Fe^{3+} is 90% larger than that around Nb^{5+} at 100 K. The elongated Pb atomic image at 100 K shown in Fig. 4 is attributable to

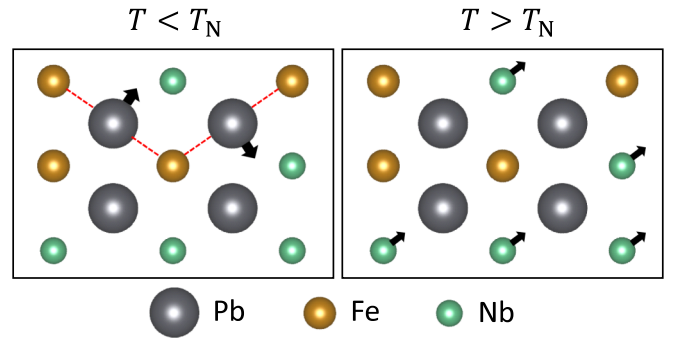


FIG. 11. Schematic illustration of the deviations from the average structure of PFN above and below T_N predicted from the present experimental results. The arrows indicate the shift of the constituent atoms, and the dashed lines in the left panel show the Fe^{3+} - Pb^{2+} - Fe^{3+} superexchange interactions.

the shift of the Pb ions around the Nb^{5+} ions located near the Fe^{3+} - Pb^{2+} - Fe^{3+} pairs.

The above discussion is in line with the previous PDF analysis study [15]. In that study, a static broadening of the PDF peak was observed at T_N , which was discussed in relation to the Pb displacement influenced by the antiferromagnetic ordering of the Fe^{3+} ions. Also, an anomalous jump in the dielectric constant at T_N reported by Yang *et al.* [7] should also have a relation to the Pb shift derived from the present XFH results.

Figure 11 schematically illustrates the deviations from the average structure described above. The arrows indicate the shift of the constituent atoms of PFN, and dashed lines express the Fe^{3+} - Pb^{2+} - Fe^{3+} superexchange interaction. Whereas the shift of the Nb^{5+} ions is remarkable above T_N in comparison with that of the Fe^{3+} ions, the shift of the Pb^{2+} ions is induced below T_N , especially between the Fe^{3+} ions, influenced by the Fe^{3+} - Pb^{2+} - Fe^{3+} superexchange interaction.

V. CONCLUSION

We performed an XFH experiment on a PFN single crystal and investigated the temperature dependence of the local structure around Nb ions from 300 to 100 K. In particular, the correlation between the Nb and the first NN Pb ions was examined in detail. In comparison with the average structure derived from single-crystal XRD measurements, the variation in the first NN Pb atomic image around the Nb ion was significant, which indicates that the Nb ion can easily shift from the center of the oxygen octahedron. Furthermore, the detailed analysis was done for the previously obtained XFH results around Fe, which shows that the local structure around Fe is similar to the average structure in the temperature range above T_N of about 150 K, in clear contrast with the local structure around Nb. These behaviors are attributable to the absence and presence of the valence electrons in the d orbitals of the Nb^{5+} and Fe^{3+} ions, respectively. On the other hand, a large positional fluctuation between the Fe and the Pb ions was confirmed at 100 K, which was attributed to the transition from the paramagnetic to the antiferromagnetic phase across T_N . This structural feature was discussed in relation to the magnetic frustration originating from the B -site randomness

and the resulting complex interactions among Fe^{3+} ions. The present study successfully elucidated the remarkable difference in the local environments around the Nb^{5+} and Fe^{3+} ions at the same B -site in PFN.

ACKNOWLEDGMENTS

This work was partially supported by a JSPS Grant-in-Aid for Transformative Research Areas (A) “Hyper-Ordered Structures Science:” Grants No. 20H05878, No. 20H05881, and No. 20H05884; Innovative Areas “Materials science on mille-feuille structure:” Grant No. 19H05126; Young Scien-

tists: Grant No. 20K15024; Scientific Research (A): Grant No. 19H00655; and Fostering Joint International Research (B): Grant No. JP19KK0124. This work was also supported by Nippon Sheet Glass Foundation for Materials Science and Engineering and Japan Association for Chemical Innovation. The XFH and powder XRD measurements were performed at BL13XU and BL02B2 of SPring-8 with the approval of the Japan Synchrotron Radiation Research Institute (JASRI): Proposals No. 2018B1297 and No. 2019A1457. The XFH experiments were also performed under the approval of the Photon Factory Program Advisory Committee: Proposals No. 2018G599 and No. 2020G581.

- [1] D. I. Woodward, J. Knudsen, and I. M. Reaney, *Phys. Rev. B* **72**, 104110 (2005).
- [2] A. A. Bokov and Z.-G. Ye, *J. Mater. Sci.* **41**, 31 (2006).
- [3] G. A. Smolenskii, A. I. Agranovskaya, S. N. Popov, and V. A. Isupov, *Sov. Phys. Tech. Phys.* **28**, 2152 (1958).
- [4] G. L. Platonov, L. A. Drobyshev, Y. Y. Tomashpolskii, and Y. N. Venevtsev, *Sov. Phys. Crystallogr.* **14**, 692 (1970).
- [5] V. A. Vokov, I. E. Mylnikova, and G. A. Smolenskii, *Sov. Phys. JETP* **15**, 447 (1962).
- [6] S.-W. Cheong and M. Mostovoy, *Nat. Mater.* **6**, 1 (2007).
- [7] Y. Yang, J.-M. Liu, H. B. Huang, W. Q. Zou, P. Bao, and Z. G. Liu, *Phys. Rev. B* **70**, 132101 (2004).
- [8] V. Bonny, M. Bonin, P. Sciau, K. Schenk, and G. Chapuis, *Solid State Commun.* **102**, 347 (1997).
- [9] N. Lampis, P. Sciau, and A. Lehmann, *J. Phys.: Condens. Matter* **11**, 3489 (1999).
- [10] S. Mabud, *Phase Transitions* **4**, 183 (1984).
- [11] S. A. Ivanov, R. Tellgren, H. Rundlof, N. W. Thomas, and S. Ananta, *J. Phys.: Condens. Matter* **12**, 2393 (2000).
- [12] S. P. Singh, D. Pandey, S. Yoon, S. Baik, and N. Shin, *Appl. Phys. Lett.* **90**, 242915 (2007).
- [13] H. Sim, D. C. Peets, S. Lee, S. Lee, T. Kamiyama, K. Ikeda, T. Otomo, S.-W. Cheong, and J.-G. Park, *Phys. Rev. B* **90**, 214438 (2014).
- [14] S. Matteppanavar, S. Rayaprol, K. Singh, V. R. Reddy, and B. Angadi, *J. Mater. Sci.* **50**, 4980 (2015).
- [15] I.-K. Jeong, J. S. Ahn, B. G. Kim, S. Yoon, S. P. Singh, and D. Pandey, *Phys. Rev. B* **83**, 064108 (2011).
- [16] M. Tegze and G. Faigel, *Nature (London)* **380**, 49 (1996).
- [17] K. Hayashi, N. Happo, S. Hosokawa, W. Hu, and T. Matsushita, *J. Phys.: Condens. Matter* **24**, 093201 (2012).
- [18] K. Hayashi and P. Korecki, *J. Phys. Soc. Jpn.* **87**, 061003 (2018).
- [19] K. M. Dabrowski, D. T. Dul, F. Firszt, A. Marasek, K. Strzalkowski, and P. Korecki, *Z. Phys. Chem.* **230**, 471 (2016).
- [20] S. Hosokawa, J. R. Stellhorn, T. Matsushita, N. Happo, K. Kimura, K. Hayashi, Y. Ebisu, T. Ozaki, H. Ikemoto, H. Setoyama, T. Okajima, Y. Yoda, H. Ishii, Y.-F. Liao, M. Kitaura, and M. Sasaki, *Phys. Rev. B* **96**, 214207 (2017).
- [21] J. R. Stellhorn, Y. Ideguchi, S. Hosokawa, N. Happo, T. Matsushita, K. Yubuta, M. Suzuki, H. Ishii, Y.-F. Liao, K. Kimura, and K. Hayashi, *Surf. Interface Anal.* **50**, 790 (2018).
- [22] K. Kudo, S. Ioka, N. Happo, H. Ota, Y. Ebisu, K. Kimura, T. Hada, T. Kimura, H. Tajiri, S. Hosokawa, K. Hayashi, and M. Nohara, *J. Phys. Soc. Jpn.* **88**, 063704 (2019).
- [23] J. R. Stellhorn, S. Hosokawa, N. Happo, K. Hayashi, T. Matsushita, N. Kawaguchi, and T. Yanagida, *Phys. Status Solidi* **257**, 2000310 (2020).
- [24] K. Hayashi, W. Saito, K. Sugimoto, K. Ohoyama, K. Hayashi, N. Happo, M. Harada, K. Oikawa, Y. Inamura, and Y. Miyazaki, *AIP Adv.* **10**, 035115 (2020).
- [25] T. Fujiwara, A. Sasahara, N. Happo, K. Kimura, K. Hayashi, and H. Onishi, *Chem. Mater.* **32**, 1439 (2020).
- [26] K. Kimura, K. Yamamoto, K. Hayashi, S. Tsutsui, N. Happo, S. Yamazoe, H. Miyazaki, S. Nakagami, J. R. Stellhorn, S. Hosokawa, T. Matsushita, H. Tajiri, A. K. R. Ang, and Y. Nishino, *Phys. Rev. B* **101**, 024302 (2020).
- [27] K. Hayashi, N. Uchitomi, K. Yamagami, A. Suzuki, H. Yoshizawa, J. T. Asubar, N. Happo, and S. Hosokawa, *J. Appl. Phys.* **119**, 125703 (2016).
- [28] T. Yamamoto, K. Hayashi, N. Happo, S. Hosokawa, and H. Tajiri, *Acta Mater.* **131**, 534 (2017).
- [29] K. Kimura, K. Hayashi, K. Hagihara, H. Izuno, N. Happo, S. Hosokawa, M. Suzuki, and H. Tajiri, *Mater. Trans.* **58**, 539 (2017).
- [30] T. Nishioka, Y. Yamamoto, K. Kimura, K. Hagihara, H. Izuno, N. Happo, S. Hosokawa, E. Abe, M. Suzuki, T. Matsushita, and K. Hayashi, *Materialia* **3**, 256 (2018).
- [31] K. Kimura, K. Hayashi, L. V. Yashina, N. Happo, T. Nishioka, Y. Yamamoto, Y. Ebisu, T. Ozaki, S. Hosokawa, T. Matsushita, and H. Tajiri, *Surf. Interface Anal.* **51**, 51 (2019).
- [32] M. Kitaura, K. Kamada, N. Happo, K. Kimura, K. Hayashi, H. Yamane, T. Ina, S. Watanabe, M. Ishizaki, and A. Ohnishi, *Jpn. J. Appl. Phys.* **58**, 120602 (2019).
- [33] S. Uechi, K. Ohoyama, Y. Fukumoto, Y. Kanazawa, N. Happo, M. Harada, Y. Inamura, K. Oikawa, W. Matsuura, F. Iga, A. K. R. Ang, and K. Hayashi, *Phys. Rev. B* **102**, 054104 (2020).
- [34] S. Hosokawa, N. Happo, K. Hayashi, K. Kimura, T. Matsushita, J. R. Stellhorn, M. Mizumaki, M. Suzuki, H. Sato, and K. Hiraoka, *J. Phys. Soc. Jpn.* **89**, 034603 (2020).
- [35] W. Hu, K. Hayashi, K. Ohwada, J. Chen, N. Happo, S. Hosokawa, M. Takahashi, A. A. Bokov, and Z.-G. Ye, *Phys. Rev. B* **89**, 140103(R) (2014).
- [36] K. Kimura, K. Yokochi, R. Kondo, D. Urushihara, Y. Yamamoto, A. K. R. Ang, N. Happo, K. Ohara, T. Matsushita,

- T. Asaka, M. Iwata, and K. Hayashi, *Jpn. J. Appl. Phys.* **58**, 100601 (2019).
- [37] K. Hayashi, C. Lu, A. K. R. Ang, K. Ohwada, Y. Xie, W. Hu, T. Matsushita, N. Happo, S. Hosokawa, A. A. Bokov, and Z.-G. Ye, *Phys. Status Solidi* **257**, 2000191 (2020).
- [38] T. Asaka, R. Matsumoto, K. Kimura, D. Urushihara, H. Ichikawa, M. Komabuchi, H. Iwama, K. Tanaka, K. Fukuda, N. Happo, K. Kakimoto, and K. Hayashi, *Phys. Status Solidi B* **257**, 2000334 (2020).
- [39] D. Oka, S. Yusa, K. Kimura, A. K. R. Ang, N. Happo, K. Hayashi, and T. Fukumura, *Jpn. J. Appl. Phys.* **59**, 010601 (2020).
- [40] S. Nakashima, Y. Fuchiwaki, N. Happo, K. Kimura, Y. Yamamoto, R. Matsumoto, K. Hayashi, and H. Fujisawa, *Jpn. J. Appl. Phys.* **59**, 010602 (2020).
- [41] A. Mesquita, B. M. Fraygola, V. R. Mastelaro, and J. A. Eiras, *Appl. Phys. Lett.* **100**, 172907 (2012).
- [42] O. Sakata, Y. Furukawa, S. Goto, T. Mochizuki, T. Uruga, K. Takeshita, H. Ohashi, T. Ohata, T. Matsushita, S. Takahashi, H. Tajiri, T. Ishikawa, M. Nakamura, M. Ito, K. Sumitani, T. Takahashi, T. Shimura, A. Saito, and M. Takahashi, *Surf. Rev. Lett.* **10**, 543 (2003).
- [43] H. Tajiri, H. Yamazaki, H. Ohashi, S. Goto, O. Sakata, and T. Ishikawa, *J. Synchrotron Radiat.* **26**, 750 (2019).
- [44] J. J. Barton, *Phys. Rev. Lett.* **67**, 3106 (1991).
- [45] See, <https://osdn.jp/projects/tmcoca/releases/p14436>.
- [46] A. X. S. Bruker, APEX3, SAINT and SADABS, Bruker AXS Inc., Madison, WI, USA.
- [47] L. Palatinus and G. Chapuis, *J. Appl. Cryst.* **40**, 786 (2007).
- [48] V. Petricek, M. Dusek, and L. Palatinus, *Z. Kristallogr.* **229**, 345 (2014).
- [49] K. Momma and F. Izumi, *J. Appl. Crystallogr.* **44**, 1272 (2011).
- [50] M. Markó, L. Cser, G. Krexner, and G. Török, *Meas. Sci. Technol.* **20**, 015502 (2009).
- [51] T. Egami, S. Teslic, W. Dmowski, P. K. Davies, I.-W. Chen, and H. Chen, *J. Korean Phys. Soc.* **32**, 935 (1998).
- [52] Y. Yoneda, K. Suzuya, and J. Mizuki, *J. Appl. Phys.* **100**, 093521 (2006).
- [53] W. Dmowski, M. K. Akbas, P. K. Davies, and T. Egami, *J. Phys. Chem. Solids* **61**, 229 (2000).
- [54] P. S. Halasyamani, *Chem. Mater.* **16**, 3586 (2004).
- [55] P. S. Halasyamani and K. R. Poeppelmeier, *Chem. Mater.* **10**, 2753 (1998).
- [56] I. P. Raevski, S. P. Kubrin, S. I. Raevskaya, V. V. Titov, D. A. Sarychev, M. A. Malitskaya, I. N. Zakharchenko, and S. A. Prosandeev, *Phys. Rev. B* **80**, 024108 (2009).
- [57] V. V. Laguta, J. Rosa, L. Jastrabik, R. Blinc, P. Cevc, B. Zalar, M. Remskar, S. I. Raevskaya, and I. P. Raevski, *Mater. Res. Bull.* **45**, 1720 (2010).
- [58] R. O. Kuzian, I. V. Kondakova, A. M. Daré, and V. V. Laguta, *Phys. Rev. B* **89**, 024402 (2014).